Smart Materials and Structures

PAPER

Theoretical and experimental investigations of a magnetostrictive electro-hydrostatic actuator

To cite this article: Yuchuan Zhu *et al* 2018 *Smart Mater. Struct.* **27** 105043

IOP Publishing
Smart Materials and Structures
Smart Mater. Struct. **27** (2017) 105043 (9pp)
https://doi.org/10.1088/1361-665X/aad071

Theoretical and experimental investigations of a magnetostrictive electro-hydrostatic actuator*

Yuchuan Zhu[1,3], Xulei Yang[1] and Norman M Wereley[2]

[1] College of Mechanical and Electrical Engineering, Nanjing University of Aeronautics and Astronautics, Nanjing 210016, People's Republic of China
[2] Department of Aerospace Engineering, University of Maryland, College Park, MD 20742, United States of America

E-mail: meeyczhu@nuaa.edu.cn, qdyangxl@163.com and wereley@umd.edu

Received 16 March 2018, revised 11 June 2018
Accepted for publication 2 July 2018
Published 20 September 2018

Abstract

In this study, the time-domain model of a magnetostrictive electro-hydrostatic actuator (MEHA) is built from the viewpoint of energy conversion, which consists of four energy transformation stages: electrical–magnetic, magneto-elastic, elastic-hydraulic and hydraulic-mechanical energy transformation. Accordingly, a Jiles–Atherton hysteresis model with the dynamic eddy current effect has been incorporated into the MEHA model, and a magneto-elastic energy transformation model has been established to depict not only the relationship between the magnetostriction and magnetization of a giant magnetostrictive material (GMM) rod, but also that between the magnetostriction and pre-stress of the GMM rod. Based on Boyle's law, an effective fluid bulk modulus equation is deduced to show a nonlinear functional relationship with fluid pressure. A pump chamber pressure model, a reed valve port flow equation model, a reed valve vibration model, a fluid pressure model in the high-pressure side cylinder, and a fluid motion model are later built sequentially to depict the complicated elastic-hydraulic transformation process. Finally, experiments show that the motion of the cylinder piston, as well as the pump flow rate, agreed well with the established model results under varying loads.

Keywords: actuator, electro-hydrostatic actuator, energy conversion, magnetostrictive material

(Some figures may appear in colour only in the online journal)

1. Introduction

Smart materials, such as piezoelectrics, electrostrictives, and magnetostrictives, have growing attraction as actuators owing to their high energy density, large blocked force, wide actuation bandwidth, and lower mechanical complexity than conventional actuators (Anderson *et al* 2003, John *et al* 2007, Zhu and Li 2014). However, the small stroke resulting from their inherent material properties have limited their further application. This situation can be overcome by implementing a smart material-based electro-hydrostatic actuator (SMEHA) (Wax *et al* 2003, John *et al* 2007, Chaudhuri *et al* 2009), which employs the frequency rectification principle to transform small amplitude and high-frequency oscillation movement of certain smart materials into large amplitude and unidirectional or bidirectional continuous movement of a hydraulic cylinder. For a review of the state of the art of this class of actuators, please see Chaudhuri and Wereley (2012).

A SMEHA typically consists of a smart material hydraulic pump (SMHP), two check valves, a accumulator and a cylinder (John *et al* 2007, Chaudhuri *et al* 2009, Chaudhuri and Wereley 2012), and the operating principle of such an SMHP is fairly similar to that of a conventional axial single-plunger hydraulic pump; nevertheless, compared with the conventional plunger pump, the plunger stroke of a SMHP is normally in the μm

---

* Research supported in part by the National Natural Science Foundation of China [grant number 51575258] and sponsored by Qing Lan Project.
[3] Author to whom any correspondence should be addressed.

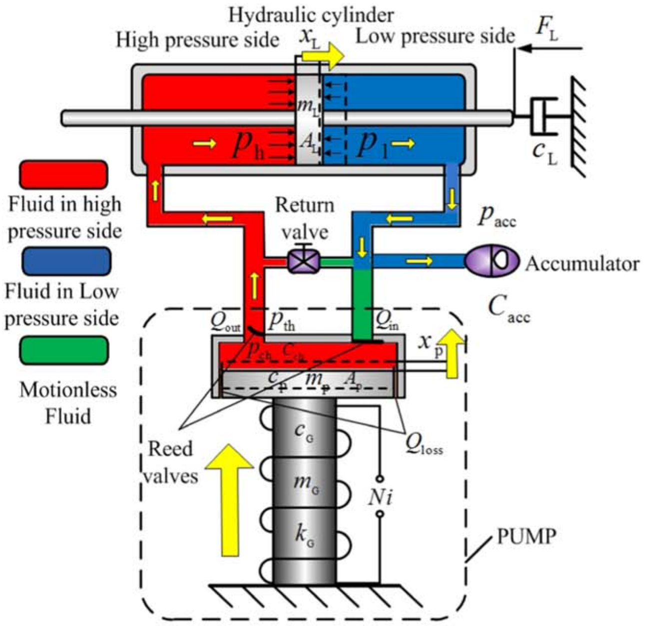

(a) Exhaust

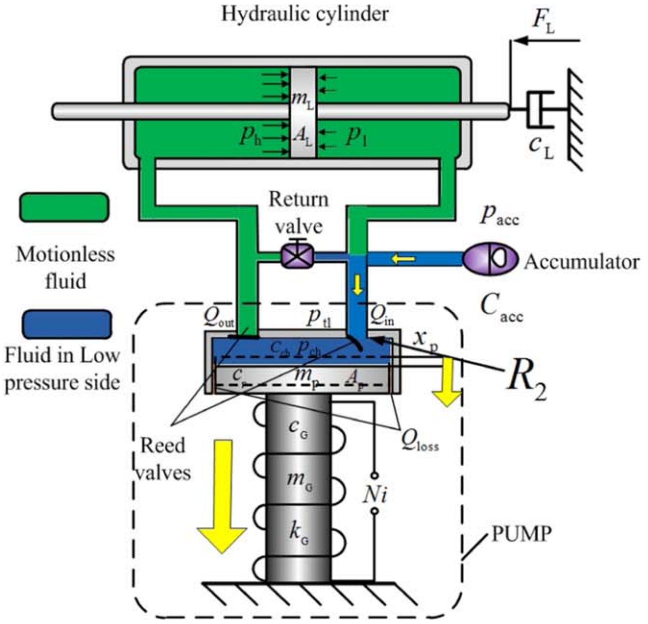

(b) Intake

Figure 1. Schematic of multi-field coupling and energy conversion in a MEHA.

range, and can only approximately reach a hundredth plunger stroke of a conventional plunger pump. Thus, this situation poses a great challenge to obtain an ideal flow efficiency and build an accurate model of a SMHP and SMEHA, because under such a small plunger stroke, many nonlinear factors such as fluid compressibility, fluid leakage and friction from the cylinder and piston would weaken the performance of a SMHP more seriously than that of a conventional plunger pump.

From an electrical signal input to output mechanical power in SMEHA, which is an extremely complicated physical process that generally involves multi-field coupling such as an electromagnetic field, stress–strain field, fluid field and thermal field; in particular, the electromagnetic coupling and the fluid–solid coupling in SMEHA play an extremely significant role in the performance of SMEHA. Accordingly, a model to depict the physical process would be especially essential to predict and optimize the performance of SMEHA. The development of a SMEHA model has been an ongoing process; the earlier models typically focus on some local properties and quasi-static performance of SMEHA. Konishi *et al* (1995) developed a simple single-degree-of-freedom (SDOF) mathematical model to design and to control the output motion of a piezoelectric stack-based actuator. Lindler *et al* (2003) presented an output power model of piezoelectric-hydraulic actuators, and Cadou and Zhang (2003) developed a simple quasi-static model to perform a reasonably good prediction of the actuator performance at frequencies below 150 Hz. Sirohi and Chopra (2003) developed a model based on the quasi-static pumping assumption and the fluid compressibility constant. Then, the various dynamic models have continued to be investigated and gradually developed, including lumped parameter approaches using electrical and mechanical analogies to model the dynamic performance of SMEHA. Nasser *et al* (2001) built a linear, lumped parameter model of the system to predict the unidirectional motion of the cylinder. A time delay associated with the mechanical response of the valves incorporated into the model which is found to be the primary limiting factor in achieving higher speed and greater power from the piezohydraulic unit. Oates and Lynch (2001), Oates *et al* (2002) established a system dynamic model of piezohydraulic pumps using MATLAB to predict the electrical–mechanical–fluid coupled behaviour of the piezoelectric pump system. The model provided a reasonable prediction of flow rate by utilizing steady-state flow analyses and assuming laminar flow. Moreover, some frequency domain dynamic models have been developed. Sirohi *et al* (2005) developed a frequency domain model to quantify the dynamics of a piezohydraulic hybrid actuator considering the effects of fluid compressibility, inertia and viscosity. Considering the piezoelectric action as a periodic force acting on a pumping membrane, (Ullmann *et al* 2000, Ullmann and Fono 2002) developed a dynamic model to predict the performance of the piezoelectric valve-less pump as a function of the frequency. Based on different approximations of the hydraulic fluid and minimizing computation effort, Tan *et al* (2005) presented two steady flow models for piezohydraulic pumps, neglecting fluid compressibility and incorporating the compressibility of hydraulic fluid. The results show that the latter provides better results under higher loads. Aiming to model the dynamic response of the passive reed valves and friction loss of the cylinder, (Chaudhuri 2008, Chaudhuri *et al* 2009, Chaudhuri and Wereley 2012) established a nonlinear time-domain model for a magnetostrictive electro-hydrostatic actuator (MEHA). The model included fluid compressibility, fluid inertia, friction of the cylinder piston, and flow losses, and it calculated the actuator flow rate well at different pumping frequencies under a free load.

In conclusion, the existing models have some limitations such as the dynamic process from input voltage to output current, the hysteresis effect and the eddy current effect in a giant magnetostrictive material (GMM) rod have not been considered in the electrical–magnetic conversion stage for a MEHA; the existing models have not focus on the situation that the bulk modulus of hydraulic oil varies with the bias pressure and the operating pressure, especially when SMEHA operated under the various load conditions; the less existing models can describe the flow rate for SMEHA under the various load. Based on this, in this paper, we formulated a time-domain model of a magnetostrictive material-based electro-hydrostatic actuator (MEHA) from the perspective of energy conversion. First, the analysis presented in this paper focuses on magnetization of a GMM rod excited by an alternating current considering both static hysteresis and dynamic eddy current effects, which have been neglected in some existing models. Second, the variational fluid bulk modulus dependence on pressure has been incorporated into the model. Third, in the fluid motion model, the fluid partial pressure loss have been put into the presented model to improve the accuracy of some previous models on the basis of energy balance point of view. Finally, the presented model can quantify MEHA flow rate whether under free load or under various load.

2. Actuator model

The established dynamic model of a MEHA involves four submodels from the viewpoint of energy conversion: the electrical–magnetic transformation model; the magneto-elastic transformation model; the elastic-hydraulic transformation model and the hydraulic-mechanical transformation model.

As shown in figure 1, a MEHA mainly consists of a GMM rod, a piston, two reed valves (one for the inlet port and the other for the outlet port), an accumulator, and a double-rod hydraulic cylinder. The GMM rod was housed by a biased solenoid coil that provides a biased magnetic field, and a driving solenoid coil for supplying alternating magnetic field. An accumulator was to provide an initial bias pressure, which is used to pressurize the fluid and ensure that the bulk modulus was sufficiently high. When the bias coil was supplied with a direct current and the driving coil was supplied with a sinusoidal current, then the deformation of the GMM rod would expand and contract in cycles, so that an oscillatory motion results at the same frequency as the sinusoidal current.

As shown in figure 1, the multi-field coupling and the energy conversion periodically appear in every operating cycle of the MEHA; thus, corresponding to the above mentioned four energy conversion processes, the electrical–magnetic energy transformation model is the dynamic magnetization model that describes the relationship between the exciting voltage and the magnetization of the GMM rod; the magneto-elastic energy model describes the relationship between the dynamic magnetostrictive strain-based displacement and the magnetization of the GMM rod; the elastic-hydraulic energy transformation model is a complex one, which involves the pump chamber pressure model, the reed valve vibration model, the fluid motion model in the pipe, the fluid dynamic pressure model in the cylinder and the accumulator dynamic model; and the hydraulic-mechanical energy transformation model describes the relationship between the dynamic hydraulic cylinder shaft displacement and the fluid pressure.

2.1. Electrical–magnetic transformation model

This stage involves the power amplifier dynamic and the inductive winding coil dynamic. The power amplifier is constant-current source to compensate for the inductance lag by an *RC* network. The inductive winding coil and power amplifier can be regarded as a second-order oscillation element, and the *RC* network can be viewed as a first-order derivative element; thus, the voltage–current conversion model can be written as the second-order linear transfer function (Zhu *et al* 2016).

$$G(s) = \frac{I(s)}{U(s)} = \frac{K\omega_n^2(1 + Ts)}{s^2 + 2\zeta\omega_n s + \omega_n^2}, \tag{1}$$

where K is the static coefficient conversion from input voltage to output current, T is the corner frequency of the *RC* network, and ω_n and ζ are the natural frequency and damping ratio of the second-order linear system describing the power amplifier and induction coil, respectively.

In this stage, the driving solenoid coil is applied by the excitation current, which first builds a magnetic field within the solenoid coil and then leads to the magnetization of the GMM rod. In our model, two physical phenomena have been considered and incorporated into the model: one is a static hysteresis effect model, and the other one is the dynamic eddy current effect model, which have been neglected by some existing models.

In a closed magnetic circuit, considering the eddy current effect in GMM rod, the applied magnetic field H generated by an alternating excitation current, i, is given by

$$H = \frac{Ni}{k_\mathrm{f} l_\mathrm{G}(1 + \tau s)} = \frac{Ni}{k_\mathrm{f} l_\mathrm{G}(1 + \mu_0 \mu_\mathrm{G} R_\mathrm{G}^2 / 4k_\mathrm{L}\rho_\mathrm{G} s)}, \tag{2}$$

where N is the number of excitation coil turns, k_f is the leakage coefficient of the magnetic flux, and l_G is the length of GMM rod, τ is the time constant caused by the eddy current, μ_0 is the permeability of a vacuum, μ_G is relative permeability of the GMM rod, and k_L is a electrical resistivity correction factor for the sheet GMM rod.

Under the actual applied magnetic field, the magnetization M can be obtained from Jiles–Atherton (1984, 1986):

$$\begin{cases} H_\mathrm{e} &= H + \alpha M \\ M &= M_r + M_i \\ M_\mathrm{r} &= c(M_\mathrm{an} - M_\mathrm{i}) \\ M_\mathrm{an} &= M_\mathrm{s}\left[\coth\left(\dfrac{H_\mathrm{e}}{a} - \dfrac{a}{H_\mathrm{e}}\right)\right] \\ M_\mathrm{i} &= M_\mathrm{an} - k\delta(1 - c)\left(\dfrac{dM_\mathrm{i}}{dH_\mathrm{e}}\right) \end{cases}, \tag{3}$$

where the parameter M_an is anhysteretic value of magnetization, M_r is the reversible value of magnetization, M_i is the irreversible value of magnetization, H_e is the total effective field, α is a mean field parameter representing inter-domain coupling, a is a parameter with the dimension of magnetic field that characterizes the shape of the anhysteretic magnetization, c is a constant that ranges from 0 (completely irreversible magnetization) to 1 (completely reversible magnetization), δ takes the value of $+1$ when H increases and -1 when H decreases, and the parameter k is the domain wall pinning constant and is used to quantify the average energy required to break the pinning site.

2.2. Magneto-elastic transformation model

The magnetostrictive rate $\lambda = \Delta\lambda/\lambda$ can describe the relative change quantity in the length of the GMM rod, which has a functional relationship with the magnetization M of the GMM rod, according to the discussion by Zhu and Li (2015). Based on the quadratic domain rotation model, the magnetostrictive rate λ can be given by

$$\lambda = \frac{3}{2}\frac{\lambda_S}{M_S^2}M^2, \tag{4}$$

where λ_S and M_S are the saturation magnetostrictive rate and the saturation magnetization, respectively.

To depict the relation between the magnetostriction of the GMM rod and the pre-stress on the GMM rod, a hyperbolic tangent function (Sun and Zheng 2006) is added to the existing quadratic domain rotation model to describe the actual magnetostriction variation by the pre-stress effect, which can be shown as follows:

$$\lambda = \begin{cases} \left(1 + \frac{1}{2}\tanh\frac{2\sigma}{\sigma_{\text{opt}}}\right)\lambda_s\frac{M^2}{M_s^2} & \sigma \leqslant \sigma_{\text{opt}} \\ \left(1 - \frac{\sigma - \sigma_{\text{opt}}}{\sigma_{\max}}\right)\left(1 + \frac{1}{2}\tanh\frac{2\sigma}{\sigma_{\text{opt}}}\right)\lambda_s\frac{M^2}{M_s^2} & \sigma > \sigma_{\text{opt}} \end{cases}, \tag{5}$$

where σ_{opt} is the optimal pre-stress on GMM rod according to the maximal magnetostrictive rate, $\sigma_{\max}$ is the maximal pre-stress on GMM rod, and σ is the actual pre-stress when GMM rod is excited by a sinusoidal magnetic field.

When the GMM rod is excited by a certain magnetic field, the magnetostrictive force generated by the GMM rod can be defined as

$$F_b = A_G E_G \lambda, \tag{6}$$

where A_G is the cross-sectional area of the GMM rod, E_G is the elasticity modulus of the GMM rod.

The pump piston motion equation is written as follows by considering it as a single-degree-of-freedom (SDOF) system:

$$\left(m_p + \frac{m_G}{3}\right)\ddot{x}_p + (c_p + c_G)\dot{x}_p + (k_d + k_s + k_G)x_p = F_b - P_{ch}A_p, \tag{7}$$

where m_p, m_G are the masses of the piston and GMM rod, respectively; c_p and c_G are the damping constants of the piston and GMM rod, respectively; k_d, k_s and k_G are the stiffnesses of the metal diaphragm, the preloaded spring and GMM rod, respectively, p_{ch} is the pressure of pump chamber; and A_p is the cross-sectional area of the piston.

2.3. Elastic-hydraulic transformation model

2.3.1. Pump chamber pressure with bulk modulus variation.

At the exhaust stage—which is shown in figure 1(a)—the outlet reed valve opens, and the inlet reed valve closes. Fluid in high-pressure side then flows from the pump chamber to the high-pressure-driven side of cylinder by the outlet tube. Subsequently, the high-pressure fluid pushes the shaft of the cylinder to move while fluid in the low-pressure side of the cylinder flows into accumulator. Conversely, in the intake stage, with the retraction of the GMM rod, the pressure in the pump chamber decreases and causes fluid flow from the accumulator to the pump chamber, which can also be described as in figure 1(b). These two stages are repeated every pump cycle, resulting in a net pump mass flow rate out by the outlet tube and an equivalent mass flow rate into the pump by the inlet tube.

To check the performance of the proposed system, a dynamic model must be formulated and analysed. At this point, the lumped parameter system model may be very useful, and it has been successfully applied to the design and analysis of many different types of physical systems.

Fluid compressibility is described by the fluid property called the bulk modulus, which is an important fluid property for determining the pump dynamic characteristics such as response time. It varies widely with pressure and temperature and depends on the ratio of entrapped air to total volume. A model for the effective bulk modulus β can be derived as follows (Sheng 1980).

$$\frac{1}{\beta} = \frac{V_a}{V_t}\left(\frac{1}{\beta_a}\right) + \left(1 - \frac{V_a}{V_t}\right)\left(\frac{1}{\beta_f}\right), \tag{8}$$

where β_a is the bulk modulus of the air under certain pressure, β_f is the bulk modulus of pure hydraulic oil, V_a is the volume of the entrapped air, and V_t is the total volume in the enclosed volume of fluid.

Boyle's law describes how the air volume tends to decrease with increasing gas pressure, which can be written as follows:

$$p_a V_a = \text{constant}, \tag{9}$$

where p_a is the pressure in the enclosed fluid, which includes hydraulic oil and the entrapped air.

The equation shows that the product of pressure and volume is a constant for a given mass of confined gas as long as the temperature is constant and the amount of gas remains unchanged within a closed system.

Deriving equation (9),

$$V_a \mathrm{d}p_a + p_a \mathrm{d}V_a = 0. \tag{10}$$

According to equation (10), the bulk modulus of the air is defined as

$$\beta_a = \frac{\mathrm{d}p_a}{\mathrm{d}V_a/V_a} = -p_a, \tag{11}$$

where '−' denotes that V_a decreases with increasing pressure p_a. Thus, regardless of the volume change direction.

$$\beta_a = p_a. \tag{12}$$

Substituting equation (12) into (8),

$$\beta = \frac{1}{\frac{V_a}{V_t}\left(\frac{1}{p_a}\right) + \left(1 - \frac{V_a}{V_t}\right)\left(\frac{1}{\beta_f}\right)}. \tag{13}$$

If the pressure value p_a is assigned to p_{acc}, accordingly, the β value can be changed to β_e, and equations (9) and (13) can be rewritten as follows:

$$p_a V_a = p_{acc} V_{acc}, \tag{14}$$

$$\beta_e = \frac{1}{\frac{V_{acc}}{V_t}\left(\frac{1}{p_{acc}}\right) + \left(1 - \frac{V_{acc}}{V_t}\right)\left(\frac{1}{\beta_f}\right)}. \tag{15}$$

Substituting equation (14) into (15),

$$\beta_e = \frac{1}{\frac{p_a V_a}{V_t}\frac{1}{p_{acc}^2} + \left(1 - \frac{p_a V_a}{V_t p_{acc}}\right)\frac{1}{\beta_f}}. \tag{16}$$

Setting $\delta_V = V_a/V_t$ denotes the percentage of entrapped air in the enclosed volume of fluid under p_a and equations (8) and (16) can be rewritten as

$$\beta = \frac{1}{\frac{\delta_V}{\beta_a} + \frac{(1-\delta_V)}{\beta_f}}, \tag{17}$$

$$\beta_e = \frac{1}{\delta \frac{p_a}{p_{acc}^2} + \left(1 - \delta \frac{p_a}{p_{acc}}\right)\frac{1}{\beta_f}}. \tag{18}$$

The fluid compliance depicts the compressibility of the fluid and can be derived by applying conservation of mass to a lumped fluid element (Cadou and Zhang 2003), which is given by:

$$C = \frac{A_p(L_p - x_P)}{\beta_e}, \tag{19}$$

where A_p is the cross-sectional area of the pump piston, x_p is the displacement of the pump piston, and L_p is the height of the pump chamber.

In the fluid pumping chamber, the pressure P_{ch} is governed by the following pressure change rate (i.e., continuity) equation inside the chamber:

$$\dot{p}_{ch} = \frac{\beta_{ech}}{A_p(L_p - x_P)}(q_{in} - q_{out} + A_p \dot{x}_P), \tag{20}$$

where q_{in} is the flow rate from the low-pressure side of pump into the chamber, q_{out} is the flow rate from the chamber into the high-pressure side of the pump, and β_{ech} is the bulk modulus of the fluid in the pump chamber.

2.3.2. Reed valve vibration model with fluid-structure coupling.

Based on Bernoulli's equation, the inlet flow rate q_{in}, and the outlet flow rate q_{out} for the pump can be written as follows:

$$q_{in} = \mathrm{sgn}(p_{tl} - p_{ch}) c_d w x_{Ri} \sqrt{\frac{2}{\rho}|p_{tl} - p_{ch}|}\ x_{Ri} = \begin{cases} x_{Ri}, & x_{Ri} > 0 \\ 0, & x_{Ri} \leqslant 0 \end{cases}, \tag{21}$$

$$q_{out} = \mathrm{sgn}(p_{ch} - p_{th}) c_d w x_{Ro} \sqrt{\frac{2}{\rho}|p_{ch} - p_{th}|}\ x_{Ro} = \begin{cases} x_{Ro}, & x_{Ro} > 0 \\ 0, & x_{Ro} \leqslant 0 \end{cases}, \tag{22}$$

where c_d is the discharge coefficient, p_{tl}, p_{th} are the pressure of the inlet reed valve side and the pressure of the outlet reed valve side, respectively. w is the area gradient, x_{Ri}, x_{Ro} are modelled as the displacement of the inlet and outlet rectification reed valve, respectively.

Both the inlet and outlet reed valves can be considered as a SDOF mass–spring–damper system in the mechanical domain. Using Newton's method of moment balance, the motion equations for the outlet and inlet rectification reed valves are

$$\begin{cases} m_{Ri}\ddot{x}_{Ri} + c_{Ri}\dot{x}_{Ri} + k_{Ri}x_{Ri} = (p_{tL} - p_{ch})A_{Rb} & p_{tL} > p_{ch} \\ x_{Ri} = 0 & p_{tL} < p_{ch} \end{cases}, \tag{23}$$

$$\begin{cases} m_{Ro}\ddot{x}_{Ro} + c_{Ro}\dot{x}_{Ro} + k_{Ro}x_{Ro} = (p_{ch} - p_{th})A_{Rb} \\ x_{Ro} = 0 \end{cases}, \tag{24}$$

where m_{Ri}, c_{Ro}, c_{Ri}, c_{Ro}, and k_{Ri}, k_{Ro} are the equivalent mass, damping, and stiffness of the inlet and outlet reed valves considering the solid–fluid coupling effect between the reed valves and hydraulic oil, respectively; and A_{Ra}, A_{Rb} are the action area on the inlet and outlet reed valves by fluid, respectively.

2.3.3. Fluid pressure in the high-pressure side of the cylinder.

Similarly, in the high-pressure chamber of the cylinder, the pressure p_h is governed by the following pressure change rate (i.e., continuity) equation.

$$\dot{p}_h = \frac{\beta_h}{A_L(l_{Lh} + x_L)}(q_{out} - A_L \dot{x}_L), \tag{25}$$

where p_h is the pressure in the high-pressure side of the cylinder, β_h is the bulk modulus of the fluid in the high-pressure side for the cylinder, A_L is the annular

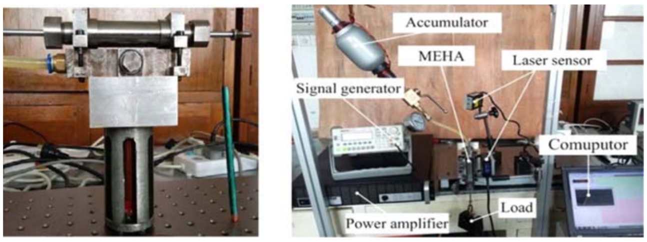

(a) MEHA prototype (b) Test rigs

Figure 2. Prototype and test rigs for a MEHA.

cross-sectional area or effective area of the piston, x_L is the piston displacement of the cylinder, and l_{Lh} is the fluid height of the high-pressure side of the cylinder.

2.3.4. Fluid motion model. Fluids from the pump chamber are rectified by the two reed valves installed in intake port and discharge port of the pump; unidirectional fluid flow is maintained in the pipeline between the reed valve and cylinder, as shown in figure 1. In a cycle, the fluid motion process consists of five stages. In the first, the fluid flows from the discharge reed valve to the high-pressure side of the cylinder; in the second, the fluid in the high-pressure side of the cylinder is compressed; in the third stage, the fluid flows from the low-pressure side of the cylinder to the accumulator; in the fourth stage, the accumulator is compressed; and in the last stage, the fluid flows from the accumulator to the intake reed valve.

In the first stage, the driving force of fluid flow is the fluid pressure difference p_{th} and p_h, which is used to resist the fluid inertia pressure drop $\Delta P_{inertia}$, the fluid viscous damping pressure drop $\Delta P_{lamimar}$ and the fluid partial pressure drop Δp_{part}. Thus, the pressure balance equation can be expressed as:

$$p_{th} - p_h = \Delta P_{inertia} + \Delta P_{laminar} + \Delta p_{part}, \tag{26}$$

$$\Delta P_{inertia} = \frac{\rho L_{th}}{A_{th}} \dot{q}_{out}, \tag{27}$$

$$\Delta P_{laminar} = \frac{128\mu_f}{\pi D_{th}{}^4} l_{th} q_{out} = \frac{8\pi\mu_f l_{th}}{A_{th}^2} q_{out}, \tag{28}$$

$$\Delta p_{part} = \frac{\rho_f}{2} \sum_{i=1}^{N=3} \left(\xi_i \frac{q_{out}^2}{A_{th}^2} \right), \tag{29}$$

where L_{th} is the fluid inertance between the discharge reed valve and the high-pressure side of the cylinder; ρ_f is the fluid density; l_{th} is the pipeline length between the discharge reed valve and the high-pressure side of the cylinder; D_{th}, A_{th} are the diameter and cross-sectional area of the pipeline, respectively; μ_f is the dynamic-viscosity coefficient of fluid, and $\xi_i (i = 1, 2, 3)$ is the damping coefficient.

By substituting equations (27)–(29) into (26),

$$p_{th} - p_h = \frac{\rho l_{th}}{A_{th}} \dot{q}_{out} + \frac{8\pi\mu_f l_{th}}{A_{th}^2} q_{out} + \frac{\rho_f}{2} \sum_{i=1}^{N=3} \left(\xi_i \frac{q_{out}^2}{A_{th}^2} \right). \tag{30}$$

In the second stage, the fluids in the high-pressure side of the cylinder are compressed, and one can write the equation to describe the situation as follows:

$$\dot{p}_h = \beta_{eh} \frac{q_{out} - \dot{x}_L A_L}{(l_0 + x_L) A_L}, \tag{31}$$

where p_h and β_{eh} are the fluid pressure and the fluid bulk modulus in high-pressure side of the cylinder, respectively, and l_0 is the initial piston position of cylinder.

In the third stage, the situation is similar to that of the first stage. Similar to equation (30), the equation can be written as follows:

$$p_l - p_{acc} = \ddot{x}_L A_L \frac{\rho_f l_{tl}}{A_{tl}} + \frac{8\pi\mu_f l_{tl}}{A_{tl}^2} \dot{x}_L A_L + \frac{\rho_f}{2} \sum_{i=1}^{N=3} \left[\xi_i \frac{(\dot{x}_L A_L)^2}{A_{tl}^2} \right]. \tag{32}$$

In the fourth stage, the dynamic pressure in accumulator can be written as follows:

$$\dot{p}_{acc} = \beta_{eacc} \frac{\dot{x}_L A_L - q_{in}}{V_a}, \tag{33}$$

where V_a is the volume of nitrogen in the accumulator, and β_{eacc} is the effective bulk modulus of fluid between the accumulator and the low-pressure side fluid of the cylinder.

In the last stage, the fluids will flow from the accumulator to the chamber of the pump, and the driving force of fluid flow is the fluid pressure difference between p_{acc} and p_{tl}. Similar to equation (30), one can write the pressure balance equation as follows:

$$p_{acc} - p_{tl} = \frac{\rho_f l_{tl}}{A_{tl}} \dot{q}_{in} + \frac{8\pi\mu_f l_{tl}}{A_{tl}^2} q_{in} + \frac{\rho_f}{2} \sum_{i=1}^{N} \left[\xi_i \frac{(\dot{x}_L A_L)^2}{A_{tl}^2} \right]. \tag{34}$$

2.4. Hydraulic-mechanical transformation model

The mass of the piston and the load, typically attached to the free end of the piston, are lumped into a single mass, m_L, based on the assumption that the piston shaft is rigid. In the simplest case, the load is purely inertial; thus, a force balance equation model can be written to depict the piston rod dynamic behaviour of the cylinder by the damping term c_L and the friction force term F_f

$$(p_h - p_l) A_L - m_L g - F_f = m_L \ddot{x}_L + c_L \dot{x}_L. \tag{35}$$

An accurate friction force model plays an important role to simulate the piston rod motion of the cylinder. The friction force originates from the friction between the outer wall of the piston and the inner wall of the cylinder tube, which typically varies with the piston velocity, accelerated velocity, temperature, load, surface roughness and material characteristics. The Karnopp model is used to describe the real friction force

$$F_f = \begin{cases} \text{sgn}(v_L) F_d, & |v_L| > v_{min} \\ \text{sgn}(v_L) \text{mi}(F, F_s), & |v_L| \leqslant v_{min} \end{cases}. \tag{36}$$

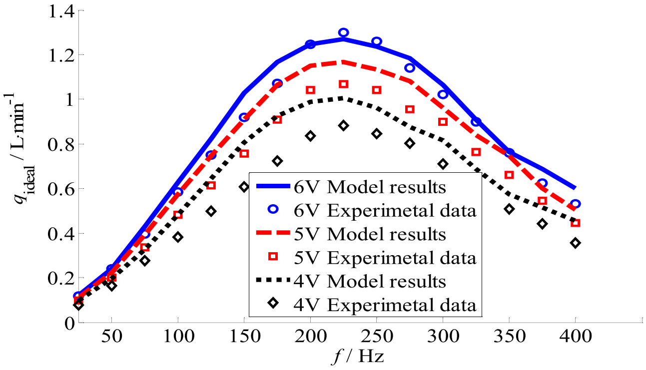

(a) p_{acc}=0.4 MPa

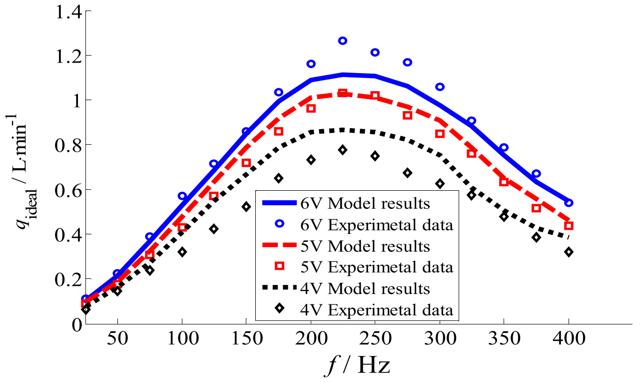

(b) p_{acc}=0.6 MPa

Figure 3. The MEHA flow rate under free load.

F_s is the maximum static friction, $F_d = 1/3F_s$ is the kinetic friction force, and v_L is the cylinder velocity.

3. Test results and model validation

3.1. Prototype and parameters

As shown in figure 2(a), a MEHA prototype is fabricated and assembled, then a test system for the MEHA is built as shown in figure 2(b). In addition, the related parameters of MEHA are shown in table 1.

3.2. The MEHA flow rate under free load

When the driving voltage peak-to-peak value is inputted as 3 V, 4 V, 5 V and 6 V, the bias voltage is accordingly inputted as 1.5 V, 2 V, 2.5 V and 3 V, respectively, the bias fluid pressure or the accumulator pressure is set to 0.4 MPa and 0.6 MPa, respectively. Based on the presented model results and the measured experimental data, the relationship between the MEHA flow rate under free load and the driving frequency is shown in figure 3.

3.3. The MEHA flow rate under various loads

The MEHA flow rate decreases with increasing load, as shown in figures 4–6, when the driving voltage peak-to-peak value is 4 V, 6 V and the bias voltage is accordingly 2 V, 3 V, respectively, the bias fluid pressure or the accumulator pressure is 0.4 MPa and 0.6 MPa, respectively, and the driving frequency is 200 Hz and 250 Hz, respectively. Based on the model results and experimental data, the actual MEHA flow rate approximate linearly decreases from

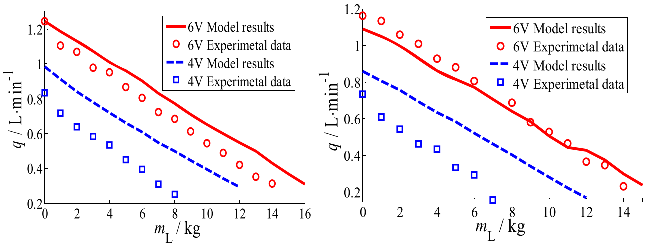

(a) p_{acc}=0.4 MPa (b) p_{acc}=0.6 MPa

Figure 4. The MEHA flow rate versus load under 200 Hz.

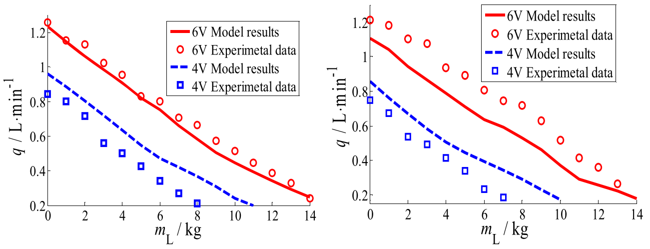

(a) p_{acc}=0.4 MPa (b) p_{acc}=0.6 MPa

Figure 5. The MEHA flow rate versus load under 250 Hz.

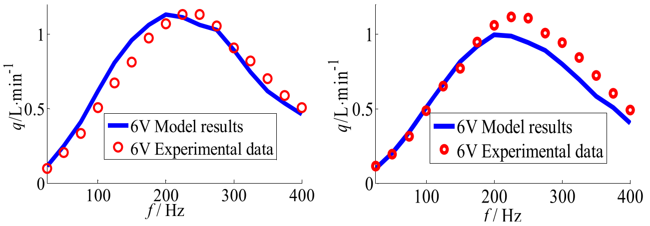

(a) p_{acc}=0.4 MPa (b) p_{acc}=0.6 MPa

Figure 6. The MEHA flow rate versus frequency under 2 kg load.

Table 1. Related parameters of MEHA.

Name	Unit	Sign	Value
GMM rod radius	mm	r_G	6.4
GMM rod length	mm	h_G	80
GMM rod relative permeability	1	μ_G	5
Permeability of vacuum	H m^{-1}	μ_0	$4\pi \times 10^{-7}$
Coil turns	1	N	1000
GMM rod elasticity modulus	GPa	E_G	14
GMM rod damping	N s m^{-1}	c_G	1.28×10^3
GMM rod mass	kg	m_G	0.12
Piston mass	kg	m_p	0.042
Pump chamber height	mm	h	0.5
Pump chamber radius	mm	r_{ch}	23.4
Fluid bulk modulus without any air	MPa	β	1800
Orifice area gradient	m	w	0.0126
Fluid density	kg m^{-3}	ρ	860
The reed valve thickness	mm	h_R	0.15

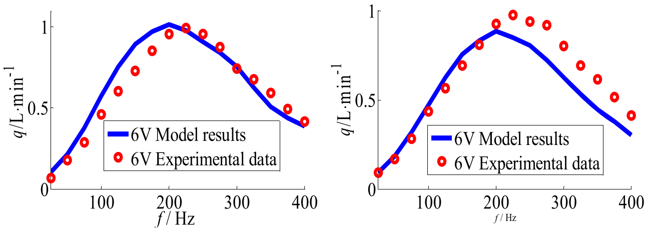

(a) p_{acc}=0.4 MPa (b) p_{acc}=0.6 MPa

Figure 7. The MEHA flow rate versus frequency under 4 kg load.

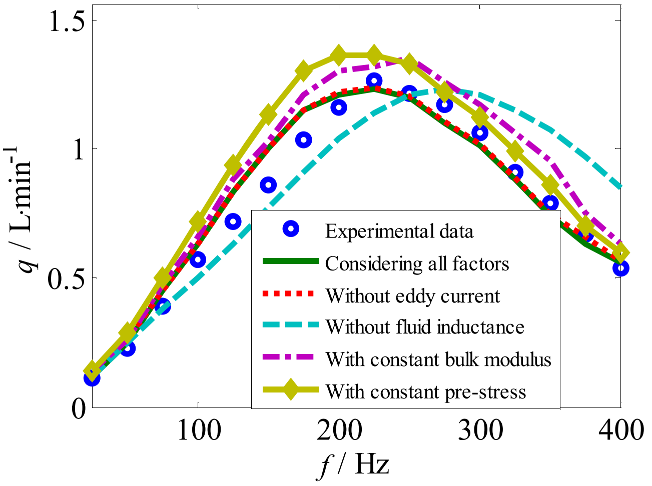

Figure 8. The MEHA flow rate versus frequency under free load.

approximately 1.2 l min^{-1} to 0 according to the load variation from 0 to 16 kg.

The MEHA flow rate increases first and then decreases with increasing frequency, as shown in figures 6–7. When the driving voltage peak-to-peak value is 6 V and the bias voltage is accordingly 3 V, the bias fluid pressure or the accumulator pressure is 0.4 MPa and 0.6 MPa, respectively, and the driving frequency varies from 0 to 400 Hz, respectively. The best frequency corresponding to the maximum flow rate for MEHA is around 225 Hz which agree figure 3 under the free load.

In addition, the MEHA flow rate and the flow rate error between the experimental data and model results considering all factors, eliminating the eddy current effect and the fluid inductance, regarding fluid bulk modulus and pre-stress as constant can clearly be shown in the figures 8 and 9.

4. Summary and conclusions

In this paper, a time-domain model of a MEHA is built from the viewpoint of energy conversion, which consists of the electrical–magnetic, magneto-elastic, elastic-hydraulic and hydraulic-mechanical energy transformation processes.

Aiming to simulate the electrical–magnetic energy transformation process, a Jiles–Atherton hysteresis model with the dynamic eddy current effect has been incorporated into the whole MEHA model, which has been neglected in some existing models. A magneto-elastic energy transformation model has been established, which can depict the relation between the magnetostriction of the GMM rod and the pre-stress on the GMM rod by adding a hyperbolic tangent function to the existing quadratic domain rotation model. In the elastic-hydraulic energy transformation model, based on Boyle's law, an effective fluid bulk modulus equation is deduced to show a nonlinear functional relationship with fluid pressure, which significantly contribute to depict the pump flow rate for MEHA under various load. Then, a pump chamber pressure model, a reed valve port flow equation model, a reed valve vibration model, a fluid pressure model in the high-pressure side of the cylinder and a fluid motion model are built sequentially to depict the complicated elastic-hydraulic transformation process. In the hydraulic-mechanical energy transformation model, a Karnopp model is used to describe the friction generated between the outer wall of the piston and the inner wall of the cylinder tube.

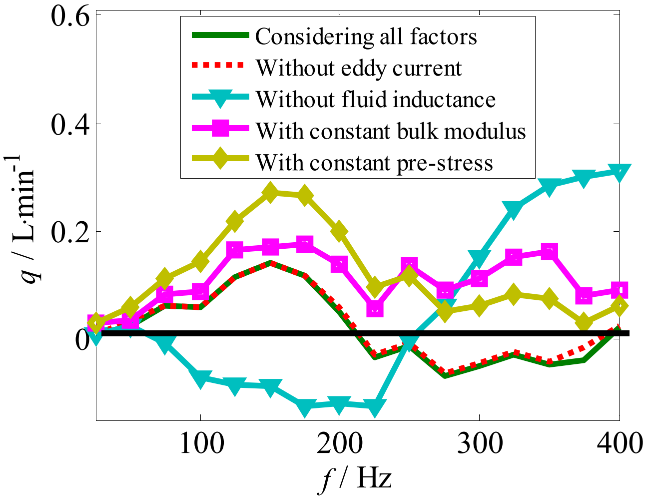

Figure 9. The MEHA flow rate error versus frequency under free load.

A MEHA prototype was fabricated and assembled, and a test system for MEHA was then built. The maximum MEHA flow rate approach 1.3 l min^{-1} under the excitation frequency 225 Hz, and the maximum MEHA blocking force is around 16 kg under 0.4 MPa bias pressure. The experimental data show that the cylinder piston displacement and the pump flow rate agreed well with the numerical results under varying loads.

ORCID iDs

Yuchuan Zhu https://orcid.org/0000-0002-7399-1656
Norman M Wereley https://orcid.org/0000-0002-9932-6988

References

Anderson E H, Bales G L and White E V 2003 Application of smart material-hydraulic actuators *Proc. SPIE* **5054** 73–84

Cadou C and Zhang B 2003 Performance modeling of a piezo-hydraulic actuator *J. Intell. Mater. Syst. Struct.* **14** 149–60

Chaudhuri A 2008 Self-contained hybrid electro-hydraulic actuators using magnetostrictive and electrostrictive materials *PhD Dissertation* Dept. of Aerospace Engineering, Univ. of Maryland, College Park MD United States of America

Chaudhuri A, Yoo J and Wereley N M 2009 Design, test and model of a hybrid magnetostrictive hydraulic actuator *Smart Mater. Struct.* **18** 085019

Chaudhuri A and Wereley N M 2012 Compact hybrid electrohydraulic actuators using smart materials: a review *J. Intell. Mater. Syst. Struct.* **23** 597–634

Jiles D C and Atherton D L 1984 Theory of ferromagnetic hysteresis *J. Appl. Phys.* **55** 2115–20

Jiles D C and Atherton D L 1986 Theory of ferromagnetic hysteresis *J. Magn. Magn. Mater.* **61** 48–60

John S, Sirohi J, Wang G and Wereley N M 2007 Comparison of piezoelectric, magnetostrictive, and electrostrictive hybrid hydraulic actuators *J. Intell. Mater. Syst. Struct.* **18** 1035–48

Konishi K 1995 Hydraulic actuators driven by piezoelectric elements *Proc. Int. Symp. on Microsystems, Intelligent Materials and Robots (Sendai, Japan,, 27–29 September 1995)*

Lindler J E, Anderson E H and Regelbrugge M E 2003 Design and testing of piezoelectric-hydraulic actuators *Proc. SPIE* **5054** 96–107

Nasser K, Vujic N, Leo D J and Cudney H H 2001 Modeling and testing of a piezohydraulic actuation system *Proc. SPIE* **4327** 354–65

Oates W S and Lynch C S 2001 Piezoelectric hydraulic pump system dynamic model *J. Intell. Mater. Syst. Struct.* **12** 737–44

Oates W S, Mauck L D and Lynch C S 2002 System dynamic modeling of a piezoelectric hydraulic pump *Proc. SPIE* **4693** 598–606

Sheng J C 1980 *Hydraulic Fluid Mechanics* (Beijing: China Machine Press) pp 292–304

Sirohi J, Cadou C and Chopra I 2005 Investigation of the dynamic characteristics of a piezohydraulic actuator *J. Intell. Mater. Syst. Struct.* **16** 481–92

Sirohi J and Chopra I 2003 Design and development of a high pumping frequency piezoelectric-hydraulic hybrid actuator *J. Intell. Mater. Syst. Struct.* **14** 135–47

Sun L and Zheng X J 2006 Numerical simulation on coupling behavior of terfenol-D rods *Int. J. Solids Struct.* **43** 1613–23

Tan H, Hurst W and Leo D 2005 Performance modeling of a piezohydraulic actuation system with active valves *Smart Mater. Struct.* **14** 91–110

Ullmann A and Fono I 2002 The piezoelectric valve-less pump-improved dynamic model *J. Microelectromech. Syst.* **11** 655–64

Ullmann A, Fono I and Taitel Y 2000 The piezoelectric valve-less pump-dynamic model *ASME J. Fluids Eng.* **123** 92–8

Wax S G, Fischer G M and Sands R R 2003 The past, present, and future of DARPA's investment strategy in smart materials *J. Miner. Met. Mater. Soc.* **55** 17–23

Zhu Y C and Li Y S 2014 Development of a deflector-jet electrohydraulic servovalve using a giant magnetostrictive material *Smart Mater. Struct.* **23** 115001

Zhu Y C and Li Y S 2015 A hysteresis nonlinear model of giant magnetostrictive transducer *J. Intell. Mater. Syst. Struct.* **26** 2242–55

Zhu Y C, Yang X L and Wereley N M 2016 Research on hysteresis loop considering the prestress effect and electrical input dynamics for a giant magnetostrictive actuator *Smart Mater. Struct.* **25** 085030